# From Graphene Nanoribbons on Cu(111) to Nanographene on Cu(110): Critical Role of Substrate Structure in the Bottom-Up Fabrication Strategy

Konstantin A. Simonov,[*,†,‡,¶] Nikolay A. Vinogradov,[†,‡,¶] Alexander S. Vinogradov,[¶]
Alexander V. Generalov,[‡,¶] Elena M. Zagrebina,[¶] Gleb I. Svirskiy,[¶] Attilio A. Cafolla,[§] Thomas Carpy,[§]
John P. Cunniffe,[§] Tetsuya Taketsugu,[∥,⊥] Andrey Lyalin,[⊥] Nils Mårtensson,[†] and Alexei B. Preobrajenski[*,‡]

[†]Department of Physics and Astronomy, Uppsala University, Box 516, 75120 Uppsala, Sweden, [‡]MAX IV Laboratory, Lund University, Box 118, 22100 Lund, Sweden, [¶]V.A. Fock Institute of Physics, St. Petersburg State University, 198504 St. Petersburg, Russia, [§]School of Physical Sciences, Dublin City University, Dublin 9, Ireland, [∥]Department of Chemistry, Faculty of Science, Hokkaido University, Sapporo 060-0810, Japan, and [⊥]Global Research Center for Environment and Energy Based on Nanomaterials Science (GREEN), National Institute for Materials Science (NIMS), Tsukuba 305-0044, Japan.

ABSTRACT Bottom-up strategies can be effectively implemented for the fabrication of atomically precise graphene nanoribbons. Recently, using 10,10′-dibromo-9,9′-bianthracene (DBBA) as a molecular precursor to grow armchair nanoribbons on Au(111) and Cu(111), we have shown that substrate activity considerably affects the dynamics of ribbon formation, nonetheless without significant modifications in the growth mechanism. In this paper we compare the on-surface reaction pathways for DBBA molecules on Cu(111) and Cu(110). Evolution of both systems has been studied *via* a combination of core-level X-ray spectroscopies, scanning tunneling microscopy, and theoretical calculations. Experimental and theoretical results reveal a significant

increase in reactivity for the open and anisotropic Cu(110) surface in comparison with the close-packed Cu(111). This increased reactivity results in a predominance of the molecular—substrate interaction over the intermolecular one, which has a critical impact on the transformations of DBBA on Cu(110). Unlike DBBA on Cu(111), the Ullmann coupling cannot be realized for DBBA/Cu(110) and the growth of nanoribbons *via* this mechanism is blocked. Instead, annealing of DBBA on Cu(110) at 250 °C results in the formation of a new structure: quasi-zero-dimensional flat nanographenes. Each nanographene unit has dehydrogenated zigzag edges bonded to the underlying Cu rows and oriented with the hydrogen-terminated armchair edge parallel to the [1−10] direction. Strong bonding of nanographene to the substrate manifests itself in a high adsorption energy of −12.7 eV and significant charge transfer of 3.46e from the copper surface. Nanographene units coordinated with bromine adatoms are able to arrange in highly regular arrays potentially suitable for nanotemplating.
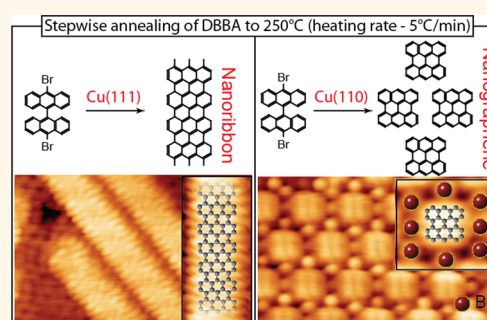
KEYWORDS: graphene nanoribbons · nanographene · Ullmann reaction · photoemission · X-ray absorption · STM · DFT

I n order to introduce a band gap into graphene structures, charge carriers can be laterally confined in quasi-one-dimensional (1D) graphene nanoribbons (GNRs).[1−6] The electronic structure of GNRs is highly dependent on their geometry and chemical composition: the one-dimensional band structure of GNRs depends critically on their chirality (armchair, zigzag, or intermediate edge shapes),[3−8] and the size of the band gap depends inversely on the GNRs' width.[3,4,8,9] Despite intriguing electronic properties, the synthesis of structurally precise GNRs using top-down concepts remains challenging.[6,9] On the other hand, a bottom-up approach presuming on-surface reactions between molecular precursors was demonstrated to be a superior for production of atomically precise GNRs.[10−25] In particular, armchair-edge GNRs with the width of seven rows of C atoms (7-AGNRs) can be grown on certain metal substrates using the 10,10′-dibromo-9,9′-bianthracene (DBBA) molecule as a precursor.

To date, this strategy was successfully implemented to prepare 7-AGNRs on

Au(111),[10,14,15,17,18] Au(788),[11,12] Ag(111),[13] and Cu-(111).[18,24,25] The growth mechanism leading to the formation of 7-AGNRs from DBBA on Au(111) and Cu(111) can be described in three steps: (i) surface-assisted dehalogenation of precursor molecules (in the case of Cu(111) followed by the formation of surface-stabilized structure); (ii) formation of linear polyanthracene chains *via* directional covalent C−C coupling of biradical molecular units; and (iii) cyclodehydrogenation reaction upon further thermal activation.

The on-surface polymerization reaction between halogen-substituted precursors, including stages (i) and (ii), is also known as the Ullmann-type coupling reaction.[26,27] It has become an established route for tailored fabrication of covalent nanostructures in the past few years. Particularly, Ullmann-type reactions were successfully utilized for the synthesis of 1D[28−31] and 2D[28,30,32−39] polymer nanostructures from suitable precursor molecules on noble metal surfaces. The structure of the resulting system is known to depend on many factors. Apart from the atomic structure of the molecular precursor itself, it is essential to take into account substrate morphology and reactivity, in order to exert full control over the formation of molecular nanoarchitectures.[21,30,35−39] The more reactive the substrate, the more pronounced its role in the bottom-up mechanism.

The bottom-up growth of GNRs is not an exception. In our recent study[18] we have shown that on the reactive Cu(111) a complete dehalogenation of DBBA takes place at room temperature (RT) and is followed by the formation of polymer chains at temperatures around 100 °C, while for the less reactive Au(111) debromination of DBBA molecules occurs at around 200 °C. Further annealing of polymer chains on Cu(111) leads to the formation of 7-AGNRs already at 250 °C, while on Au(111) the formation of GNRs completes only at 400 °C. This difference confirms the crucial role of substrate properties, including its atomic structure and reactivity, in the GNR synthesis mechanism. It is well known that the properties of noble metal surfaces are strongly dependent on their composition and face orientation. In particular, density functional theory (DFT) calculations indicate that the surface reactivity increases with the decreasing coordination of surface Cu atoms in the series Cu(111), Cu(110), Cu(100).[40,41] The correlated upward energy shift of the d-band center can cause stronger hybridization between the metal d-states and the molecular orbitals of adsorbates, thus increasing the chemisorption strength. Therefore, a change in the surface orientation can dramatically affect the molecular−substrate interaction. For the particular case of the benzotriazole molecule, densely packed surfaces are not reactive enough to interact with the molecular π system, while the reactivity of the Cu(110) surface is sufficient to promote such an interaction.[40] Moreover, it was experimentally demonstrated that the

highly anisotropic Cu(110) surface can induce a 1D structure growth;[29,31,42] therefore one could potentially anticipate formation of spatially aligned GNRs on this substrate. For this reason it is of great interest to compare the on-surface reaction mechanisms accompanying the adsorption and temperature-induced modification of DBBA molecules on Cu(111) and Cu(110).

In this work we address the question of how a change in the atomic structure of the copper substrate from close-packed (111) to open (110) affects the on-surface reaction pathway for a DBBA molecule, which in the case of DBBA/Cu(111) ultimately leads to the formation of 7-AGNRs. Will it result in the growth of aligned GNRs on Cu(110), or will a completely different scenario be enforced by the change in surface symmetry and reactivity? To answer these questions, we have performed a comparative study of DBBA adsorption and transformation on Cu(111) and Cu(110) by using near-edge X-ray absorption fine structure (NEXAFS) spectroscopy, X-ray photoelectron spectroscopy (XPS), and scanning tunneling microscopy (STM) in combination with DFT calculations. This set of complementary techniques allows us to follow and understand all reaction steps accompanying the system evolution in the temperature range from −120 to 250 °C. We report on a radical difference in the thermally induced evolution of the DBBA/Cu(111) and DBBA/Cu(110) systems. It is demonstrated how and why a variation in the substrate reactivity and anisotropy leads to a change in dimensionality of the resulting nanostructures from quasi-1D on Cu(111) to quasi-0D on Cu(110).

RESULTS

It has been shown previously that surface-assisted debromination of DBBA molecules on Cu(111) is already complete at RT.[18] In the present study the Br 3d photoemission (PE) spectrum has been recorded in the sample temperature range starting from −120 °C in order to follow the debromination reaction progress. The resulting intensity maps, showing the evolution of the Br 3d line for DBBA deposited on Cu(111) and Cu(110), are presented in Figure 1a,b, respectively. As can be seen from Figure 1, the debromination dynamics is significantly different for the two copper surfaces. Below −40 °C, the Br 3d signal from DBBA/Cu(111) (Figure 1a) is mainly a single broad spin−orbit doublet with the binding energy (E_B) of Br $3d_{5/2}$ = 70.4 eV, while the corresponding spectrum of DBBA/Cu(110) (Figure 1b) consists of two doublet components of almost equal intensity: one is again located at E_B(Br $3d_{5/2}$) = 70.4 eV and another at E_B(Br $3d_{5/2}$) = 68.5 eV. A low-E_B spin−orbit doublet appears in the Br 3d spectrum of DBBA/Cu(111) at a temperature of approximately −30 °C. This is accompanied by a proportionate fast decrease of the high-E_B component, which completely
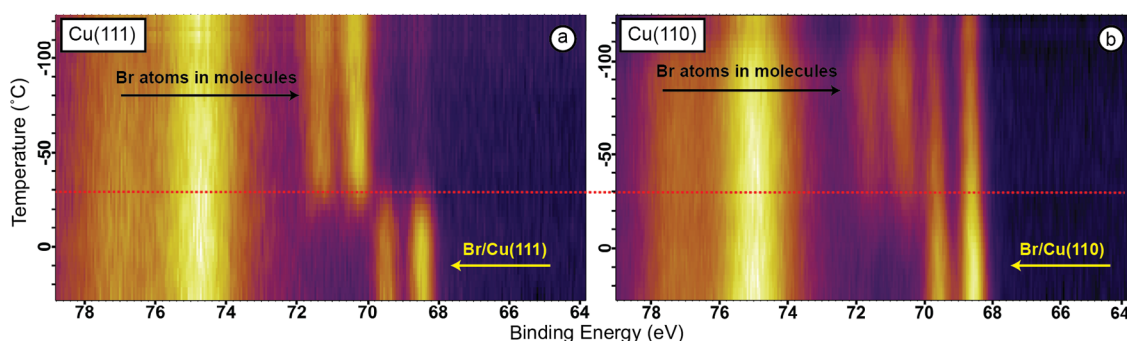
Figure 1. Intensity maps, showing evolution of the Br 3d XPS spectra of DBBA/Cu(111) (a) and DBBA/Cu(110) (b) taken with hv = 170 eV, as a function of increasing sample temperature. Temperature varies from −120 to 30 °C. The red dashed line marks the temperature of −30 °C. XPS intensity between 74 and 78 eV is due to the Cu 3p signal.

disappears above −25 °C. In turn, the total intensity of the Br 3d line changes insignificantly in the entire studied temperature interval, being simply redistributed from the high-E_B to low-E_B component at around −30 °C. In the case of DBBA/Cu(110) annealing above −30 °C also extinguishes the high-E_B energy component, leaving behind a single doublet at E_B(Br 3d$_{5/2}$) = 68.5 eV, the intensity of which is increased by the amount close to the intensity of the disappeared component.

The low-E_B component with E_B(Br 3d$_{5/2}$) = 68.5 eV in Figure 1a corresponds to atomic Br, adsorbed on Cu(111).[18] Since the intensity pattern observed for DBBA/Cu(111) strongly resembles that for DBBA/Au(111) but with an offset of almost 200 °C, it is logical to assume that the component at E_B(Br 3d$_{5/2}$) = 70.4 eV is due to Br atoms bonded to the anthracene units of DBBA on Cu(111). This conclusion finds further confirmation in the fact that both low- and high-E_B components are shifted by the same value of 0.7 eV to higher binding energy in comparison with corresponding components of DBBA on Au(111) (67.8 and 69.7 eV, respectively). The E_B positions of the Br 3d components for DBBA on Cu(111) and on Cu(110) are the same; therefore the above identification of spectral components is valid also for DBBA on Cu(110). A conservation of the total Br 3d intensity upon heating from −120 °C to +30 °C for both substrates indicates that Br desorption is insignificant in this temperature range. This can be explained by a strong bonding between chemisorbed Br adatoms and active copper surfaces, which suppresses the temperature-activated Br desorption that is observed for DBBA/Au(111).[18,19]

From Figure 1 one can see that at −120 °C the DBBA molecules stay intact on Cu(111), while partial debromination takes place on Cu(110). This is a clear indication of increased surface reactivity and stronger DBBA−substrate interaction on the Cu(110) surface as compared to the close-packed Cu(111). Since the intensity ratio between two Br 3d doublets for DBBA on Cu(110) is close to unity below −40 °C (Figure 1b), it is plausible to assume that the DBBA molecule loses one of its two Br atoms on this substrate. Heating both surfaces does not have any remarkable impact on the molecule until the temperature reaches −30 °C. Above this temperature a fast debromination of DBBA/Cu(111) takes place, and at −25 °C the molecule loses both Br atoms simultaneously. In contrast, on Cu(110) the molecule is already half-debrominated at −120 °C, while complete debromination takes place at the same temperature as on Cu(111) (−25 °C). The reason for this effect is a high reactivity of copper in atomic rows along the [1−10] direction of Cu(110), which causes a substitution of one C−Br bond in DBBA by a C−Cu bond with very low activation barrier (this occurs at temperatures as low as −120 °C or maybe even lower). Strong bonding to the Cu row atoms may result in tilted adsorption geometry, with one anthracene subunit flat and bonded to the surface and the other one pointing upward, thus increasing the distance between its Br atom and the surface. This explains why the second Br atom remains bonded to DBBA until −30 °C, when the thermal motion allows it to come close enough to the Cu(110) surface to initiate complete debromination.

DFT modeling of the DBBA adsorption on Cu(111) and Cu(110) corroborates our experimental findings. Figure 2a,b shows the relaxed configuration of DBBA/Cu(111), and the DBBA adsorption energy (as defined in the SI) is determined to be E_{ads} = −2.14 eV. The adsorption geometry is governed by the tendency to keep each anthracene subunit in DBBA as parallel to the flat Cu(111) surface as possible. The molecular axis passing through the C−C bond connecting two anthracene subunits is thus parallel to the substrate. In turn, both bromine atoms belong to the molecule and are located at a distance of about 3 Å from the copper substrate. Nevertheless, the steric hindrance between hydrogen atoms causes significant deformation of both anthracene subunits, as can be seen in Figure 2b.

In contrast to Cu(111), one of the most favorable DBBA adsorption geometries on the Cu(110) surface implies spontaneous surface-assisted partial debromination of the molecule even at low temperatures
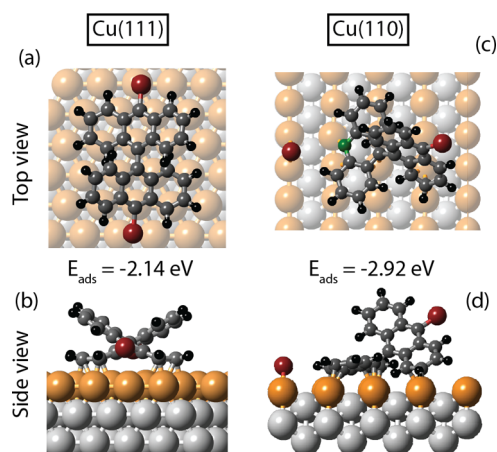
Figure 2. Optimized geometries computed within DFT for the initially intact DBBA molecule on Cu(111) (a, b) and Cu(110) (c, d) at 0 K. E_{ads} refers to the calculated adsorption energy of the molecule (a, b)/molecular fragment (c, d). Bromine atoms are wine-colored, carbon atoms are dark gray (except for the debrominated carbon, which is green), and hydrogens are black. The surface substrate atoms are light brown, while the deeper layers are light gray.

(Figure 2c,d). In this case one of the C—Br bonds in DBBA can be broken with the subsequent formation of a new C—Cu bond when a Br atom originally bonded to an anthracene subunit occasionally comes into the vicinity of the low-coordinated copper in the [1−10] rows. As can be seen from Figure 2c,d this causes a significant change in the adsorption geometry of the DBBA and leads to a 0.78 eV increase in the absolute value of adsorption energy relative to the DBBA/Cu(111) system. The debrominated anthracene subunit is lying on two neighboring [1−10] rows almost parallel to the surface, while the halogenated anthracene unit is tilted at an angle of about 60° relative to its "flat-lying" counterpart. This in turn results in a significant increase in the distance between the remaining Br atom of the DBBA molecule and the Cu(110) surface and consequently in a higher temperature stability of the corresponding C—Br bond, in agreement with the above Br 3d XPS data analysis.

The debromination process is one of the most important stages for the Ullmann reaction, which is the first step leading to the formation of GNRs on Cu(111). Therefore, the differences revealed in the debromination pathway for DBBA on Cu(111) and Cu(110) are the first indication of the strong influence of the substrate properties on the entire subsequent on-surface reaction mechanism.

A comparison of the STM images corresponding to DBBA/Cu(111) and DBBA/Cu(110) at RT is shown in Figure 3. At this temperature the process of C—Br bond cleavage is completed, and STM reveals a significant difference between structures generated from DBBA on Cu(111) (Figure 3a) and Cu(110) (Figure 3b): on Cu(111) the debrominated DBBA molecules form long chain-like structures, while on Cu(110) highly ordered 2D islands are observed.
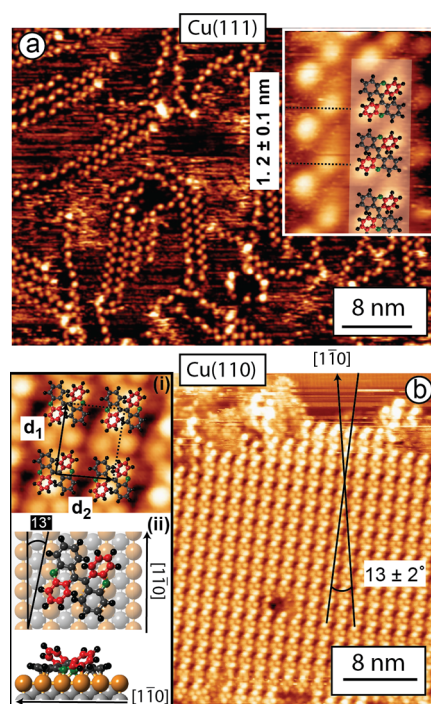

Figure 3. (a) STM image of surface-stabilized organometallic chains made of debrominated DBBA molecules on Cu(111) at RT. The inset shows a schematic model of these molecules superimposed over the chain. Additional circular features that are visible to the right in the inset image are Br atoms appearing on the Cu(111) surface, as a result of DBBA debromination. (b) STM image of debrominated DBBA molecules forming an island on Cu(110) at RT and surrounded by Br adatoms. Black solid lines show the orientation of molecules with respect to the [1−10] Cu rows. The insets, from top to bottom: (i) enlarged image of the island's unit cell with overlaid models of molecular fragments, (ii) calculated ground-state adsorption configuration of a single debrominated DBBA, top and side views. On all insets the ball-and-stick models of debrominated DBBA are additionally color coded to distinguish carbon atoms linked to Cu (green atoms) and anthracene lobes looking upward (red atoms). All other atoms are color coded as in Figure 2. Tunneling parameters (V_S/I_T): (a) −0.61 V/0.1 nA; (b) +1 V/150 pA.

Considering the DBBA/Cu(111) system (Figure 3a), the protrusions appearing on both sides of the chain axis result from the opposite tilt of the anthracene subunits in DBBA analogous to the tilt characteristic for intact molecules on Cu(111) (Figure 2b). The inset in Figure 3a shows an enlarged image of two chains, with molecular models superimposed on one of them (see figure caption for explanation). From analysis of multiple images, the periodicity along the chain axis is determined to be 1.2 ± 0.1 nm, which is significantly larger than the period characteristic of covalent polyanthracene chains (0.85 nm).[10] Therefore, it was concluded that at RT the debrominated DBBA molecules form surface-stabilized organometallic chains on Cu(111).[25] Analogous organometallic structures were demonstrated to be intermediates for Ullmann reaction-based synthesis of various polymer structures on Cu(111).[29,31,33,37]

In contrast, on Cu(110) the molecular units form 2D islands instead of 1D chains, although a small fraction

of a disordered phase is also present in the images. To facilitate understanding of the island structure, it should be noted that at RT the molecular fragments are assumed to bind to the copper substrate at both debrominated sites. Hence, the adsorption geometry of DBBA/Cu(110) at RT resembles that for DBBA/Cu(111) with two diagonally located anthracene lobes tilted away from the surface. This is supported by the DFT calculations presented below. Therefore, each debrominated DBBA molecule is expected to give two bright maxima in the STM image. The inset (i) in Figure 3b shows an enlarged image of the island structure with overlaid ball-and-stick models of DBBA units. In principle, one can observe two possible island types, corresponding to the opposite tilt of anthracene subunits within the DBBA molecule (see Figure S1a,b in the SI). To a certain extent these are just mirror reflections of each other; therefore we consider only one domain type, represented in Figure 3b. The unit cell is close to rectangular with the parameters $d_1 = 2.0 \pm 0.1$ nm and $d_2 = 1.5 \pm 0.1$ nm. This means that, unlike the DBBA on Cu(111), the formation of C—Cu—C bonds connecting individual molecular fragments into organometallic chains can be excluded. Indeed, the distance between neighboring molecules along the molecular axis (along d_2) is about 1.5 nm, which would result in an impossibly large C—Cu bond length of approximately 4 Å. The island additionally comprises clearly visible circular protrusions surrounding the twisted molecular units, which we attribute to chemisorbed Br atoms detached from the molecules at RT. Similar adsorption of halogen atoms after dissociation from the molecule was observed previously.[29,31,32,43] Moreover, as reported by Kuck et al.,[43] the halogen atoms can promote molecular ordering on Cu(111). In Figure 3b one can see a region of clean Cu(110) surface in the upper-right corner of the image, with close-packed Cu rows along the [1−10] crystallographic direction. Apparently, the DBBA anthracene subunits are not oriented parallel to the Cu rows, but rotated in the surface plane by $13 \pm 2°$ with respect to the [1−10] direction (see Figure 3b).

The top and side views of the DFT-calculated geometry for dehalogenated DBBA on Cu(110) are presented in inset (ii) in Figure 3b. The complete surface-catalyzed dehalogenation of DBBA is accompanied by the binding of the second anthracene subunit to the copper surface via bonding of debrominated carbon with the copper atom in the underlying [1−10] row (shown as second green carbon atom). This in turn results in a relatively flat adsorption conformation of DBBA having two anthracene lobes (red-colored) partially tilted away from the surface, in agreement with the STM data discussed above. The DBBA fragment in the calculated ground-state geometry is oriented at an angle of 13° with respect to the Cu(110) rows, also in full agreement with experiment. The whole molecular
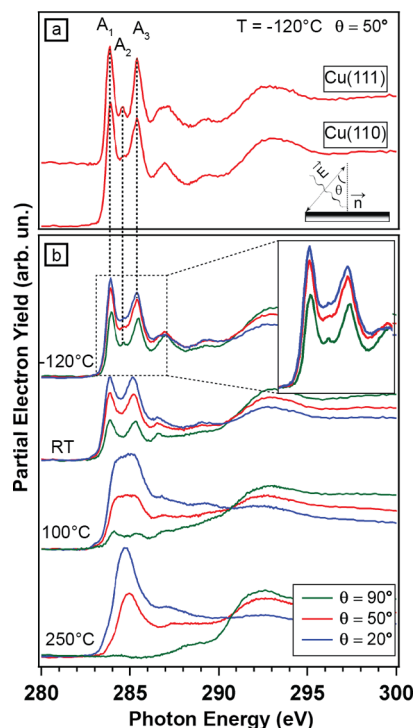

Figure 4. (a) Comparison of C K-edge NEXAFS spectra of DBBA/Cu(111) and DBBA/Cu(110) at −120 °C, $\theta = 50°$. (b) Evolution of angle-dependent NEXAFS spectra of DBBA/Cu(110) upon annealing to the noted temperatures for 15 min. θ is an angle between the light polarization vector and surface normal (see inset in (a)). The inset in the top-right corner in (b) shows the enlarged π^* region of the spectrum at −120 °C.

fragment is then oriented in such a way that both anthracene subunits are locked to the [1−10] rows in a symmetrical way, causing a significant increase in adsorption energy from −2.92 eV for the half-debrominated molecule to −4.97 eV after complete debromination.

To conclude this section, the formation of 1D organometallic chains is not favorable on Cu(110). Instead, warming from −120 °C to RT induces the growth of 2D islands, composed of individual debrominated molecules bonded to the [1−10] rows through both of the dangling bonds.

Figure 4a compares the C K-edge NEXAFS spectra from DBBA deposited on Cu(111) and Cu(110) at −120 °C. Although the near-edge fine structure regions of both spectra are similar and dominated by the π^* resonances A_1 and A_3, which originate from the anthracene subunits,[44] the relative intensity of additional resonance A_2 significantly decreases for DBBA/Cu(110). Taking into account that resonance A_2 reflects the C 1s → π^* transitions localized on the C atoms bonded to Br,[18] it is natural to associate this decrease with partial (half) debromination of DBBA on Cu(110) at −120 °C, while on Cu(111) the molecules remain intact. This is in agreement with our above conclusions based on the analysis of Br 3d PE data (Figure 1).

Figure 4b shows angle-dependent C K-edge NEXAFS spectra characteristic of the four consecutive stages of

DBBA evolution on Cu(110) upon heating from −120 to 250 °C with 15 min annealing at 100 and 250 °C. By comparing the spectral curves shown in red, taken at an intermediate angle of $\theta = 50°$ between the light polarization vector and the surface normal, one can see that the annealing results in dramatic changes in the π^* region, thus indicating pronounced variations in the atomic and electronic structure of the sample. The overall behavior of the temperature evolution of the C K-edge spectra is very similar to that for DBBA/Cu(111) in the same temperature range:[18] at RT peak A_2 is missing, while at 250 °C the separate absorption resonances merge into a single broad band. The absence of peak A_2 starting from RT is in line with the analysis of Br 3d PE spectra and is a consequence of the complete debromination of the molecules. Moreover, by analogy with DBBA/Cu(111) it is reasonable to assume that heating to 250 °C activates the cyclode-hydrogenation within the molecular fragments, thus leading to the formation of a delocalized π^* system, which manifests itself as a broad absorption band.

An angle dependence is seen at all annealing steps. It is generally characterized by a reduction or complete suppression of π^* resonance intensity at normal incidence ($\theta = 90°$) and its enhancement at grazing incidence ($\theta = 20°$). However, as can be seen from the inset in Figure 4b, peak A_2 behaves differently: it is prominent in the normal incidence geometry (green curve) and almost absent at grazing incidence (blue curve). This angular dependence is consistent with the "tilted" adsorption geometry of the molecule at −120 °C discussed above. Indeed, the carbon atom bonded to the remaining Br atom is responsible for the appearance of peak A_2. According to our DFT calculations, it resides on the anthracene subunit, which is not parallel to the Cu(110) surface, but forms an angle of around 60° with it. Therefore, the angle dependence of resonance A_2 should have an opposite character in comparison with A_1 and A_3, leading to the observed effect.

For the C K-edge spectrum at RT the angle dependence is more pronounced, indicating a less tilted geometry upon complete debromination, although the π^* resonances still have a significant nonzero intensity at normal incidence. Such behavior is a result of the alternating tilt of the anthracene subunits in the debrominated molecular fragment, which additionally supports our interpretation of STM data for DBBA on Cu(110) at RT (Figure 3b) and is in agreement with the results of DFT simulations (Figure 3b, inset (ii)). For the C K-edge spectrum at 250 °C the π^* resonance is absent in the normal incidence geometry. This observation suggests a flattening of the system as a consequence of cyclodehydrogenation within the molecular fragment. An analogous cyclodehydrogenation process within the polyanthracene chains leads to the formation of GNRs on Cu(111), which are characterized by a

very similar C K-edge spectrum at 250 °C.[18] In turn, the C K-edge spectrum from DBBA/Cu(110) at 100 °C represents an intermediate step between RT and 250 °C. As can be seen, the system is significantly flattened, but the cyclodehydrogenation process is not complete. This is different from the DBBA/Cu(111) system, where NEXAFS and STM did not reveal any evidence for cyclodehydrogenation at 100 °C.[18,25] On the contrary, for DBBA/Cu(111), annealing to 100 °C eliminates the metal-stabilized organometallic chains and induces the formation of covalent polyanthracene chains.[25] In contrast to DBBA/Cu(110), the C K-edge spectrum from polymer chains on DBBA/Cu(111) is dominated by sharp π^* resonances A_1 and A_3.[18] Only further annealing at 150 °C induces partial cyclodehydrogenation within the polymer chains on Cu(111), which manifests itself as a C K-edge spectrum similar to that for DBBA/Cu(110) at 100 °C.[18]

The above-noted difference in the NEXAFS spectra for DBBA on Cu(111) and Cu(110) annealed at 100 °C allows us to suggest that debrominated DBBA cannot form polymer chains on the active Cu(110) surface. This can also be confirmed by STM images from DBBA/Cu(110) after annealing at 100 °C, which provide no evidence of covalent coupling between DBBA fragments on Cu(110) (see Figure S2 in the SI). On the contrary, partially flattened DBBA fragments remain well separated from each other.

Since no polymer chains can be formed on the Cu(110) surface before cyclodehydrogenation starts, it is reasonable to expect that annealing to 250 °C will result in different structures for DBBA/Cu(111) and DBBA/Cu(110). In support of this, Figure 5 shows STM images obtained after a 15 min anneal of DBBA on Cu(111) (a, b) and Cu(110) (c) at 250 °C. In agreement with earlier publications,[18,25] on Cu(111) annealing leads to the formation of long (up to 50 nm) 7-AGNRs (Figure 5a). From Figure 5a and, to a lesser extent, Figure 5b, it can be seen that the GNRs are surrounded by adatoms. These atoms can be associated with Br atoms chemisorbed on the Cu(111) surface resulting from DBBA debromination. This is supported by Br 3d PE data, which reveal the presence of Br species on the Cu(111) surface up to 500 °C.[18] It should be noted that we do not observe the growth of isolated Br islands on the free Cu(111) surface.[46] On the contrary, Br atoms tend to agglomerate in the vicinity of GNRs, where they most likely can be trapped in the surface potential modulated by the presence of chemisorbed nano-ribbons. A similar effect has been recently utilized for adatom capture on metal surfaces.[42,45] Nevertheless, further away from GNRs the Br atoms self-assemble in a regular $(\sqrt{3} \times \sqrt{3})R30°$ structure, characteristic of a submonolayer of Br on Cu(111).[46]

Interestingly, under certain conditions (like those shown in Figure 5a), the GNRs on Cu(111) can exhibit an additional zigzag modulation of their edge.
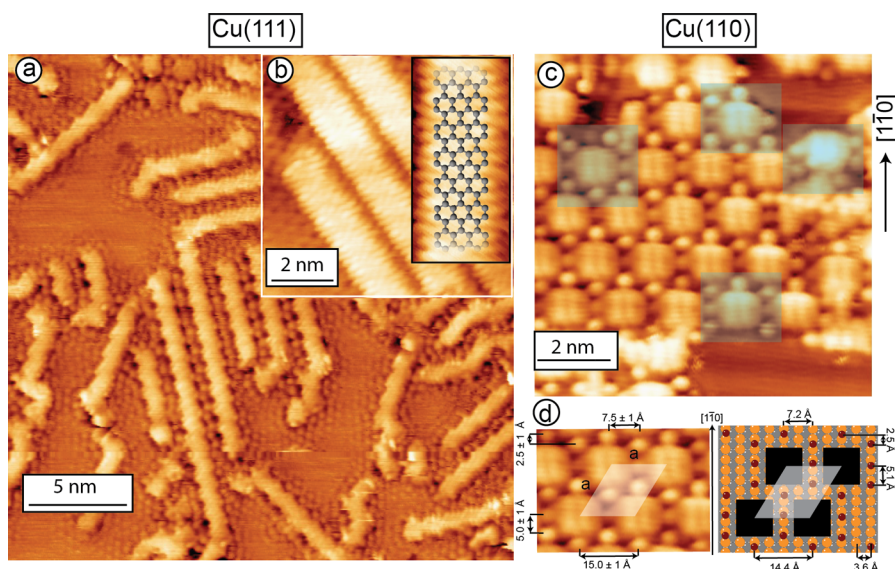
Figure 5. STM images obtained after a 15 min anneal at 250 °C, showing 7-AGNRs on Cu(111) (a, b) as well as square nanographenes formed on Cu(110) (c). The circular features on all images were determined to be Br adatoms (see text for explanation). Inset in (b): enlarged image of individual 7-AGNR, revealing the charge density distribution along the ribbon edge superimposed with the corresponding structural model. In (c): semitransparent square areas indicate sites where irregularities in Br surrounding NG units are visible. (d) Part of the STM image in (c), showing individual unit cells of the periodic structure (left), shown together with the corresponding structural model (right) built on the basis of the STM image. The nanographene units are represented as black squares of appropriate size, the Br atoms are wine-colored, and the surface atoms and atoms of deeper layers of the substrate are light brown and light gray, respectively. Tunneling parameters (V_S/I_T): (a) −0.04 V/170 pA, (b) −0.04 V/770 pA, (c) +0.77 V/580 pA.

Different explanations were proposed to describe this effect, advocating either chiral GNR structure[24] or standard armchair structure.[25] In line with our previous studies,[18,25] we believe that the growth of GNRs on Cu(111) can result only in armchair ribbons, which is further indirectly supported by STM images in the inset of Figure 5b. Here an individual C−H bond can be seen on the ribbon edges, while the edge modulation is much less pronounced even though the ribbons are the same as in Figure 5a. Although the nature of the edge modulation is not entirely clear, it may be attributed to the effect of regularly situated Br adatoms surrounding GNRs. Even more probable, since the GNRs strongly interact with the Cu(111) surface, this effect can result from the presence of chemically nonequivalent regions along the GNR due to the periodically varying strength of the ribbon−substrate interaction. Further detailed investigations, supported by theoretical calculations, are necessary for a complete understanding of this effect.

In contrast to the case of Cu(111), the adsorption of DBBA on Cu(110) and subsequent stepwise heating to 250 °C leads to the formation of individual square units, instead of GNRs (Figure 5c). The size of each molecular unit, measured from STM images, is about 9 Å × 9 Å, which corresponds to the dimensions of a single DBBA molecule. Taking into account that annealing at 250 °C results in cyclodehydrogenation within the DBBA molecular fragment accompanied by a flattening of the molecule, each unit can be considered as a quasi-0D regular graphene dot with the area close to 1 nm², which hereafter will be called nanographene (NG). At least two different types of coexisting regular arrangements of NGs were observed in the STM images, showing a more dense hexagonal or less dense square ordering. The ratio between different types of NG ordering depends on the preparation conditions, although the densest hexagonal phase shown in Figure 5c appears to be predominant when the coverage is close to one monolayer.

In both arrangements, one of the edges of NG (although from Figure 5c it is impossible to say exactly which, zigzag or armchair) is parallel and another one is perpendicular to the [1−10] direction. As can be seen from Figure 5c and d (left), the NGs within the ordered region arrange in a hexagonal pattern with a unit cell basis vector $a = 1.5 \pm 0.1$ nm. Each of the NGs is coordinated by eight regularly spaced adatoms. In cases where there is a deviation from the ideal structure (see for example areas marked by blue semitransparent rectangles in Figure 5c), even more adatoms can surround a single NG unit, while at the cluster edge the adatoms may diffuse away. It is reasonable to assume that these adatoms have the same origin as those observed at RT for DBBA/Cu(110) (Figure 3b) and at 250 °C for DBBA/Cu(111) (Figure 5a), and hence they are identified as bromine atoms. Moreover, bromine chemisorbed on the Cu(110) surface can be detected in XPS up to 550 °C (Figure S3). Nevertheless, on the basis of STM images alone, the possibility that the protrusions between the NGs are related to native Cu adatoms cannot be excluded either. Indeed, as recently

demonstrated by Haq et al.,[42] Cu adatoms may play a crucial role in the on-surface synthesis of macromolecular organometallic structures from nonhalogenated molecules on the Cu(110) surface. On the other hand, in line with our above discussion of DBBA on Cu(110) at RT, the formation of C—Cu—C bonds between individual NGs via Cu adatoms can be ruled out because the spacing between them is too large.

In order to completely exclude misinterpretation of the adatom nature, we have performed a cross-check experiment with 9,9′-bianthracene (BA) molecules, which contain no Br atoms (i.e., DBBA molecules with Br substituted by H). It has been found that no structure like the one shown in Figure 5c can be formed with BA molecules on Cu(110) annealed to 250 °C. By analogy with DBBA, the BA molecules also fuse into square NG-like units via cyclodehydrogenation upon annealing. On the other hand, no circular features, which would coordinate the NGs in a way similar to that described previously, were observed (Figure S4b in the SI). Therefore, we are confident that in the case of DBBA precursors the adatoms, captured in the vicinity of NG units, are Br atoms chemisorbed on Cu(110).

As determined from DFT simulations, the most energetically preferable positions for Br adsorption on Cu(110) are the short-bridge sites between the Cu atoms in the [1−10] rows. With this in mind and using the distances measured from STM images, an atomic model of the bromine matrix, in which NG units are incorporated, can be constructed (Figure 5d, right). This schematic model is in perfect agreement with the experimental data. It clearly shows that each of the NG units occupies approximately three [1−10] rows and is well separated from the nearest neighbors. In turn, the Br adatoms are regularly placed between them.

Although the orientation of the square NG unit relative to the [1−10] rows of Cu(110) cannot be determined exactly from Figure 5c, the adsorption of NG with its armchair edge almost parallel to the [1−10] direction can be demonstrated to be the most energetically favorable configuration for individual debrominated NG units on Cu(110) (Figure S6a). However, it is shown below that the real situation is more complicated, because the NG units experience partial dehydrogenation of their edges upon annealing.

An insight into the chemical state of individual carbon atoms constituting the DBBA precursor upon formation of the NG can be gained from the C 1s XPS spectra recorded for different annealing temperatures. As can be seen from Figure S5 in the SI, the line shape evolves gradually upon annealing from RT to 150−200 °C, while further annealing to 350 °C does not change the spectrum very much, which confirms the stability of the system in this temperature range. Figure 6a,b,c show, respectively, fitted C 1s XPS spectra for debrominated DBBA/Cu(110) at RT and NG/Cu(110) after 250 °C annealing, compared with the C 1s XPS line

for GNRs/Cu(111) obtained after annealing at the same temperature. The same fitting procedure used previously for investigations of GNRs on Au(111) and Cu(111) was implemented for the analysis of NG formation on Cu(110) (see ref 18 for details). In general it entails a deconvolution of the C 1s peak into several components with the relative intensities matched to the fraction of atoms in chemically close positions (see structural models in Figure 6a,b,c). By analogy with DBBA on Cu(111), the 28 C atoms constituting the debrominated DBBA molecule on Cu(110) can be divided into three main groups (see the corresponding inset in Figure 6a): C atoms with three neighboring carbons and sp^2-hybridized valence electron states, C[C$_3$] sites (black carbon atoms); C atoms in C[C$_2$H] sites (cyan carbon atoms); and C atoms that have lost their Br and, as shown above, are liable to interact with Cu, C[C$_2$] (green carbon atoms). Consequently, the C 1s XPS spectrum can be fitted with three components, C1 (284.6 eV), C2 (284.2 eV), and C3 (283.3 eV), corresponding to C atoms in C[C$_3$], C[C$_2$H], and C[C$_2$] sites, respectively. In the case of DBBA on Cu(111), stepwise annealing of debrominated DBBA to 250 °C results in the formation of AGNRs, characterized by the C 1s XPS spectrum constituting only two components: C1 and C2 (Figure 6c). The C1 component dominates the spectrum, accounting for about two-thirds of the total peak area in accordance with the corresponding structural model (see inset to the left). In turn, the C 1s XPS spectrum from nanographene on Cu(110) (Figure 6b) is characterized by a significantly more pronounced low-E_B shoulder, which develops as a clearly distinguishable plateau-like structure with approximately half the maximum intensity of the main peak. Hence it is hardly possible to realize a physically justified fitting procedure for the C 1s spectrum from NG/Cu(110) with only C1 and C2 components. Instead, to unambiguously fit the photoemission line, it is necessary to include a new component (C4), shifted by 0.5 eV to lower binding energy with respect to C2 and thus contributing to the low-energy shoulder. The appearance of component C4 in the C 1s XPS spectrum of NG/Cu(111) is associated with edge carbon atoms that have lost their hydrogens and have bonded to copper substrate atoms (C[C$_2$Cu] sites). Indeed, C 1s components with the same energy have been previously observed for partially decomposed GNRs/Cu(111) annealed above 400 °C and were associated with the dehydrogenated edge carbon atoms interacting with the Cu(111) substrate.[18] Furthermore, a similar low-E_B shift was measured for the C atoms on the edges of graphene nanoislands.[47] Thus, we suggest that unlike Cu(111), where no such effect can be observed upon annealing to 250 °C, on the more active Cu(110) substrate the temperature-activated surface-assisted dehydrogenation reaction, leading to the formation of additional C—Cu bonds, accompanies the cyclodehydrogenation
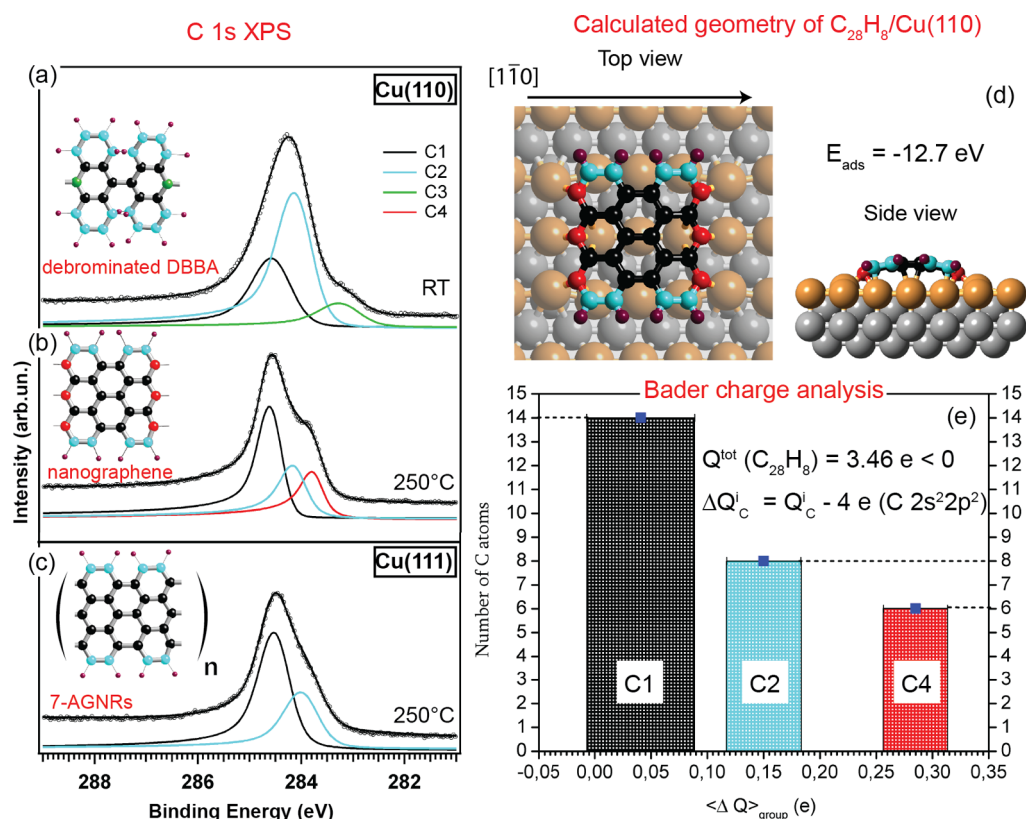
C 1s XPS

Calculated geometry of C$_{28}$H$_8$/Cu(110)

Figure 6. Left panel: C 1s XPS spectrum for DBBA/Cu(110) at RT (a) and after stepwise annealing to 250 °C (b) together with a C 1s line corresponding to GNRs/Cu(111) after 250 °C annealing (c); hv = 380 eV. Each line is fitted in accordance with its structural model; see insets to the left. The colors of the atoms in the model correspond to the colors of the spectral components. Right panel: (d) The most energetically profitable configuration of the nanographene C$_{28}$H$_8$, which has lost four hydrogen atoms as a result of surface-catalyzed dehydrogenation reaction upon 250 °C annealing, as predicted from C 1s XPS and determined within DFT. The strong binding of C atoms (red) to the favorably located underlying copper [1−10] rows results in a very high adsorption energy of E_{ads} = −12.7 eV. The atoms within NG are color-coded to correspond with the inset in (b). The surface atoms and atoms of deeper layers of the Cu(110) substrate are light brown and light gray, respectively. (e) Results of the Bader analysis applied to the charge density distribution for the calculated configuration (d). Calculations yield the total electron transfer of Q_{tot} = 3.46e from the Cu(110) substrate to the adsorbed nanographene. The average extra Bader charge $\langle \Delta Q \rangle_{group}$ can be calculated for the carbon atom belonging to each of three groups responsible for C1 (14 black atoms), C2 (8 cyan atoms), and C4 (6 red atoms) components in the spectrum of nanographene. For each individual carbon atom (i) ΔQ^i_C corresponds to the difference between the calculated total valence electrons charge (Q^i_C) and the charge of valence electrons in carbon's elemental state (four electrons in $2s^2 2p^2$ valence configuration): $\Delta Q^i_C = Q^i_C - 4e$. Therefore, on the histogram in (e) the height of the column, centered at the calculated value of $\langle \Delta Q \rangle_{group}$ (blue squares), corresponds to the number of carbon atoms in each group, and the width of the column corresponds to the doubled value of standard deviation for ΔQ within the group.

in the DBBA fragment. It is worth noting that the debrominated C atoms, giving rise to the C3 component for DBBA/Cu(110) at RT, are not distinguishable from the dehydrogenated carbon atoms after nanographene formation and, thus, also contribute to the intensity of the C4 component. A shift to higher E_B on going from C3 to C4 can be due to a redistribution of the excess electron density localized on the debrominated C atoms in the DBBA molecule over the whole carbon framework upon formation of fused nanographene with a delocalized electronic structure.

Integrated intensities of the C1, C2, and C4 components in the C 1s XPS spectrum are in the ratio 1:0.55:0.42, which implies that within an individual nanographene unit there are 14, 8, and 6 carbon atoms in the C[C$_3$], C[C$_2$H], and C[C$_2$Cu] sites, respectively. Taking into account that two of the carbon atoms

forming bonds with the Cu substrate are debrominated, the fitting analysis allows us to assume that annealing to 250 °C leads to the dehydrogenation of four additional edge C atoms, leaving behind the molecular fragment C$_{28}$H$_8$. Although the exact location of these four C atoms in the molecule is generally unknown, the most energetically favorable configuration of the nanographene unit with four H atoms removed can be calculated by DFT. Calculated ground-state structures of debrominated nanographene (C$_{28}$H$_{12}$) on Cu(110) have been used as a starting point for optimization of the dehydrogenated system. The largest energy gain has been obtained for the system with dehydrogenated C atoms located on the zigzag edges of NG. In this case the NG unit orients with its armchair edge parallel to the [1−10] direction as a result of an interaction with underlying [1−10] copper rows (see Figure S6b for
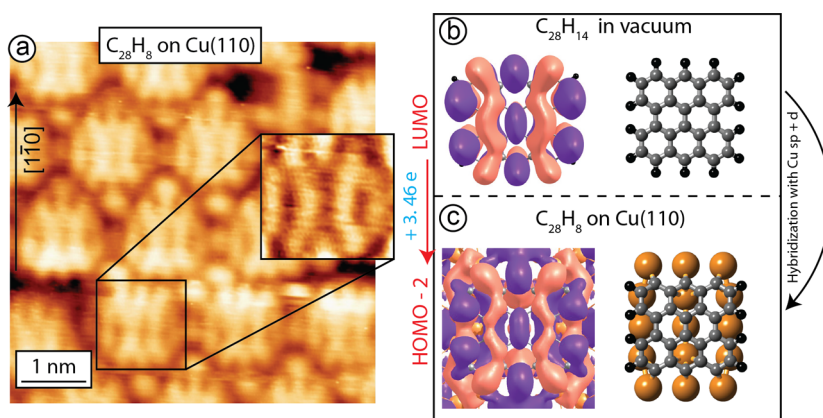
Figure 7. (a) Small-scale, high-resolution STM image showing hexagonally arranged nanographenes on Cu(110) surrounded by Br adatoms (round features). Tunneling parameters (V_S/I_T): −0.1 V/500 pA. Unlike Figure 5c, the image reveals a local density distribution of occupied states within individual nanographene units, as additionally illustrated by the inset. (b and c) LUMO and HOMO−2 (dichromatically colored isosurfaces to the left), calculated for isolated hydrogen-terminated NG and NG/Cu(110) (ball-and-stick models to the right), respectively. The isosurfaces represent the constant value of the real part of the wave function and reflect the shape of the charge density isosurfaces (the isovalue is 0.02 e/Å^3 in (b) and 0.01 e/Å^3 in (c)). The coloring of the isosurfaces is based on the wave function sign.

further information). The inset in Figure 6b shows a schematic model of the NG unit, where C atoms that have lost their Br and H neighbors and are engaged in an interaction with Cu atoms are colored in red (NG with stoichiometry $C_{28}H_8$).

Figure 6d shows top and side views of the calculated ground-state adsorption configuration for dehydrogenated NG on Cu(110). The carbon atoms are color-coded in correspondence with the C 1s peaks in the XPS fitting procedure. As can be seen, in this geometry the six carbon atoms shown in red and located on both zigzag edges of the NG can interact with well-positioned copper atoms in three underlying [1−10] rows, resulting in a very high adsorption energy of −12.7 eV. The hydrogen-terminated armchair edges are aligned parallel to the [1−10] direction, in agreement with the STM data discussed above (Figure 5c,d).

The Bader topological analysis has been further applied to the electron density distribution corresponding to the ground-state configuration determined from DFT. The outcome is illustrated in Figure 6e. The pronounced interaction with Cu(110) results in a significant negative charge transfer of $Q^{tot} = 3.46e$ per NG unit from the underlying substrate. Furthermore, we have performed analysis of Bader partial charges on individual carbon atoms (ΔQ^i_C) within each of three groups (black-, cyan-, and red-colored carbon atoms), which contribute to the peaks C1, C2, and C4 in the C 1s XPS spectrum of nanographene (Figure 6b). As can be seen from Figure 6e, the clear difference in the average extra Bader charge per carbon atom ($\langle\Delta Q\rangle_{group}$) exists between the atoms responsible for the different components. The $\langle\Delta Q\rangle_{group}$ is negative for all three groups, and its absolute value increases in the order black atoms—cyan atoms—red atoms. This is in agreement with the suggested explanation for the origin of the C 1s photoemission line shape of nanographene presented

above. Indeed, since the electron transfer from the substrate is largest for carbon atoms in the C[C$_2$Cu] sites, the corresponding component will have the smallest binding energy due to the additional screening of the core hole created upon the photoemission process. In general, the more electron charge located on the carbon atom, the less the corresponding C 1s binding energy. Therefore, the atoms in C[C$_3$] sites carrying the smallest electron charge will, on average, contribute to the high-E_B component, while the C 1s electrons of the atoms in C[C$_2$H] sites (cyan-colored) should have an intermediate value of binding energy. Taking into account the number of carbon atoms in each group, one can expect that the C 1s photoemission spectrum from the calculated structure (Figure 6d) will be in close agreement with the experimentally observed spectrum (Figure 6c). In this way calculations unambiguously support our interpretation of experimental data and *vice versa*.

Figure 7a shows a small-scale STM image of the hexagonal NG island structure recorded with a very low negative bias voltage. In this case the tunneling conditions allow us to image the local charge density distribution of the filled states in the vicinity of the Fermi level within individual NG units (see inset in Figure 7a). A direct comparison with the molecular orbitals calculated for isolated nanographene fully terminated with H atoms reveals a close similarity between the experimental STM image (Figure 7a) and the lowest unoccupied molecular orbital (LUMO) (Figure 7b, also calculated in ref 21). Apparently, unoccupied states cannot be imaged in STM at negative sample voltages. However, as predicted above, the interaction of NG units with Cu(110) results in electron transfer to the NG, enabling a transformation and shift of the LUMO below the Fermi level. In order to understand the effect of interaction with the substrate on the electronic
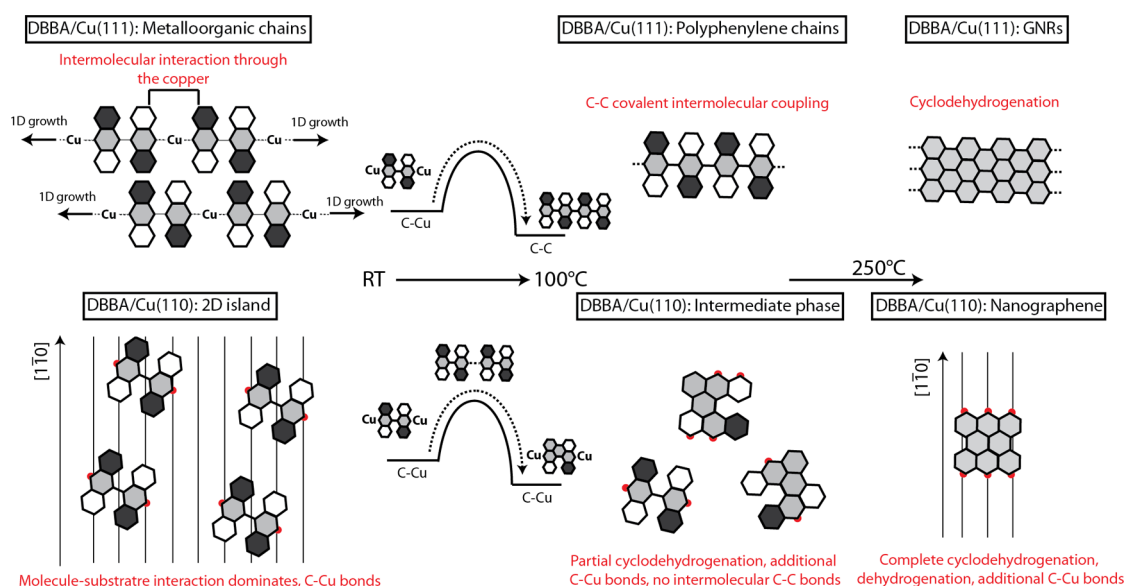
Figure 8. Schematics summarizing and comparing the on-surface reaction pathways for DBBA on Cu(111) and Cu(110). At RT and 100 °C stages the benzene rings constituting DBBA molecules and other molecular derivatives are color coded to show the geometrical distortion: white color corresponds to the tilt toward the substrate, while the dark gray represents the lobes directed away from the surface; light gray has been chosen for the intermediate regions. The red circles on the edges of DBBA/Cu(110) illustrate the bonding of the edge C atoms of the DBBA fragment with the copper atoms in the underlying [1−10] rows. For further description refer to the text.

structure of NG, the molecular orbitals have been additionally calculated for NG adsorbed on Cu(110) in the ground-state geometry suggested above (Figure 7c, right). The highest occupied molecular orbital (HOMO)−2 of the adsorbed NG (Figure 7c, left) clearly resembles the LUMO of isolated hydrogen-terminated nanographene and is thus responsible for the observed STM contrast. It is important to note that a match between the STM image and the calculated HOMO−2 orbital is possible only if the NG is oriented with its armchair edge parallel to the [1−10] rows, as predicted by DFT and shown in Figure 6d.

Apparently, the LUMO of isolated NG becomes populated and shifts to HOMO−2 for NG/Cu(110) due to the electron transfer from the Cu(110) surface, as predicted by the Bader charge analysis.

DISCUSSION

The experimental and theoretical results described above demonstrate a significant difference between the on-surface reaction pathways for the DBBA molecule on two copper facets. On Cu(111) the Ullmann reaction and further cyclodehydrogenation result in formation of AGNRs. On the other hand, on Cu(110) square nanographenes strongly bonded to the substrate are formed as a result of cyclodehydrogenation within DBBA fragments accompanied by a partial dehydrogenation of the NG edges. In the previous section we have investigated each stage of the on-surface reaction taking place on Cu(110) and its resulting products. We now briefly summarize our knowledge about both systems and reveal principal factors that modify the mechanism of the DBBA on-surface

transformation on Cu(110). Accordingly, Figure 8 provides a schematic comparison between the bottom-up processes on the two copper surfaces. On the basis of this scheme, let us consider each of the three steps: RT, 100 °C, and 250 °C.

Heating from −120 °C to RT causes a complete debromination of DBBA on both surfaces, leading to the formation of the surface-stabilized structures with DBBA fragments bonded to copper at the debrominated sites. However, on Cu(111) the precursors form 1D organometallic chains, while on Cu(110) the DBBA fragments are well separated from each other and bonded to the copper atoms in [1−10] rows (the corresponding locations of C−Cu bonds for DBBA/Cu(110) are shown by red circles in Figure 8).

We propose that the growth of 1D organometallic chains is governed by the surface-assisted intermolecular interaction between the debrominated DBBA fragments. In other words, each DBBA unit, which at RT can easily diffuse on the flat Cu(111) surface, attempts to form a bond with the copper atom already activated by the C−Cu bond formation with another molecule. Despite not being observed in STM, the participation of native Cu adatoms in organometallic bonding cannot be excluded. The chain growth direction is determined by the azimuthal orientation of the debrominated molecule on Cu(111) and results in alignment of the chains along six preferred high-symmetry directions.[18,24] It is also proposed that the organometallic chains are further stabilized by a noncovalent side-by-side interaction within patches constituting several chains, as shown schematically in Figure 8.

In contrast to Cu(111), where the intermolecular interaction determines the growth of 1D organometallic chains, the interaction of DBBA with the anisotropic Cu(110) surface is the main factor responsible for the formation of 2D islands. As shown schematically in Figure 8, each DBBA fragment adopts an orientation promoting easiest bonding of the debrominated carbon atoms to the copper atoms in the [1−10] rows. Therefore, the debrominated DBBA fragments appear to be anchored in the preferential adsorption sites through two C−Cu bonds.

Annealing at 100 °C modifies both systems, although in different ways (see Figure 8). As illustrated by the respective schematic energy diagrams, for DBBA/Cu(111) temperature activation promotes a dissociation of the C−Cu bonds and overcomes the barrier for covalent intermolecular bond formation. The subsequent interlinking of debrominated DBBA units results in polyanthracene chains, the final product of the Ullmann reaction. In turn, annealing DBBA on Cu(110) at 100 °C is sufficient to break the C−Cu bonds and (due to higher activity of Cu(110)) to activate the process of cyclodehydrogenation within DBBA fragments. The associated flattening reduces the possibility of covalent coupling between the units due to the increased steric hindrance relative to the intact (nondehydrogenated) DBBA molecules. This can also be understood as an increase in the barrier for covalent bond formation. Moreover, strong spatial variation of the potential of the anisotropic Cu(110) surface makes the C−C interlinking of the DBBA fragments unfavorable. Indeed, unlike Cu(111), where the DBBA fragment freely diffuses in the shallow potential of the close-packed (111) surface, on Cu(110) a molecular fragment that has left its adsorption position instantly seeks to repin with the [1−10] rows. Consequently, an annealing of DBBA/Cu(110) at 100 °C results not in the polymer chains but in a mixture of debrominated DBBA fragments and poorly ordered partially flattened nanoflakes, all bonded to the [1−10] rows through their debrominated and partly dehydrogenated edges. Thus, the Ullmann reaction does not take place for DBBA on Cu(110), and no polymer chains can be grown. In general, this makes it impossible to fabricate nanoribbons on Cu(110), at least using a preparation procedure analogous to that employed to grow GNRs on Cu(111) and Au(111),

where the polymer chains play the role of precursor for the growth of GNRs.

Further heating to 250 °C activates the cyclodehydrogenation within polymer chains on Cu(111), thus leading to the growth of quasi-1D GNRs. In contrast, on Cu(110) the cyclodehydrogenation within DBBA accompanied by the partial dehydrogenation of molecule edges results in the formation of quasi-0D nanographenes. Nanographenes have a $C_{28}H_8$ stoichiometry, are bonded to the [1−10] rows along their zigzag edges, and are oriented with the H-terminated armchair edge along the [1−10] direction.

CONCLUSIONS

It can be concluded that a fine balance between the precursor-substrate and intermolecular interactions is essential for the growth of GNRs. For the Ullmann reaction, underlying the GNRs bottom-up synthesis, the properties of the metal substrate are crucial. The covalent coupling between precursor molecules can be either enabled or blocked on surfaces having the same elemental composition but different atomic structure. In particular, unlike a close-packed Cu(111) surface, the Cu(110) surface is strongly anisotropic, which affects the adsorption energy, diffusion barriers, and lateral interactions of the molecular precursors.

By using a combination of complementary experimental techniques underpinned by a theoretical analysis, we have studied the on-surface transformations of DBBA molecules on both Cu(111) and Cu(110). Unlike Cu(111), where the Ullmann reaction between the debrominated DBBA fragments results in formation of polymer precursors for GNRs after 100 °C annealing, on Cu(110) the beginning of cyclodehydrogenation and the highly anisotropic surface potential block the covalent coupling of the molecular units, and thus no polyanthracene chains are formed. As a result, instead of GNR growth, a stepwise annealing of DBBA on Cu(110) to 250 °C leads to the formation of nanographenes ($C_{28}H_8$ flat derivatives of DBBA) oriented with their armchair edge parallel to the [1−10] direction. Each NG unit is strongly bonded to the underlying [1−10] copper rows, causing a significant electron transfer from the substrate. Moreover, NG on Cu(110) can self-assemble into ordered arrays, which may be interesting for nanotechnological applications, *e.g.*, nanotemplating.

METHODS

Experimental Methods. The temperature evolution of the system upon controllable annealing was monitored by XPS, NEXAFS, and STM. The spectroscopic data were obtained at the D1011 beamline, MAX IV (Lund, Sweden). The STM results were acquired using the MAX IV laboratory STM system (VT STM XA, Omicron Nanotechnology GmbH, Lund, Sweden) and cross-checked in a separate analogous STM system (group of

Dr. A. A. Cafolla, DCU, Dublin, Ireland). The same *in situ* preparation procedures were used in all experimental stations. The Cu(111) and Cu(110) crystals were cleaned by several cycles of Ar^+ sputtering ($E(Ar^+)$ = 1 keV) at RT and subsequent annealing in UHV at 550 °C. The cleanliness of the substrate was verified either by XPS and low-energy electron diffraction (LEED) or directly by STM. The preliminary outgassed DBBA molecules (Angene Chemical 99% purity) were deposited by sublimation

under UHV conditions from a home-built Knudsen cell onto the clean substrate maintained at either liquid nitrogen temperature (−120 °C measured with a thermocouple in contact with the substrate) or RT. The amount of deposited material was monitored by XPS and STM and was less than a monolayer. Further, on both surfaces the molecules were gradually heated to (i) RT, (ii) 100 °C, and (iii) 250 °C for 15 min with a heating rate of about 5 °C per minute and were fully characterized at each step. For the comparative experiment with 9,9′-bianthracene molecules (99% purity) the Knudsen-cell evaporator was exchanged in order to prevent contamination with residual Br. The C K-edge NEXAFS spectra were measured in partial electron yield (PEY) mode implying a retarding potential, U_{ret}, of −150 V at the entrance of the PEY detector in order to increase the signal-to-background ratio. The C K-edge NEXAFS spectra were normalized to the corresponding spectrum of the pristine substrate taken over the same energy range. The photoelectron spectra were measured relative to the Fermi level of the system in the normal emission geometry and normalized to the current in the storage ring and number of scans. The photon energy resolution at the C K-edge was set to 75 meV, and the resolution of the SES-200 electron analyzer was set to 125 meV for the C 1s and Br 3d photoelectron spectra. The peak-fit analysis of the C 1s XPS spectra was performed with the FitXPS software.[48] The base pressure during spectroscopic measurements was better than 5×10^{-10} mbar. The STM measurements were performed at liquid nitrogen temperature in an analysis chamber with a base pressure of 5×10^{-11} mbar. The images were recorded in constant-current mode using an electrochemically etched polycrystalline tungsten tip. The voltage, V_S, corresponds to the sample bias with respect to the tip. The WSxM software[49] was used for the processing of STM images.

Computational Details. The calculations were carried out using DFT with the gradient-corrected exchange−correlation functional of Wu and Cohen (WC)[50] as implemented in the SIESTA package.[51] The WC functional provides an adequate description of the lattice constants, crystal structures, and surface energies of solids and systems with layered structures such as graphene or hexagonal boron-nitride (h-BN) monolayers deposited on 3d, 4d, and 5d transition-metal surfaces.[52,53] Double-ζ plus polarization function (DZP) basis sets were used to treat the valence electrons of all atoms, while the core electrons were represented by Troullier−Martins norm-conserving pseudopotentials.[54] Periodic boundary conditions were used for all systems, including free molecules.

The Cu fcc lattice was optimized using the Monkhorst−Pack[55] $14 \times 14 \times 14$ k-point mesh for Brillouin zone sampling. The calculated Cu lattice parameter, $a = 3.625$ Å, is in excellent agreement with the experimental value of $a = 3.61496$ Å.[56] The optimized lattice of bulk Cu was used to construct a four-layer 8×8 slab for Cu(111) and an eight-layer 5×8 slab for Cu(110) surfaces, containing 256 and 320 Cu atoms, respectively. The periodically replicated slabs were separated by a vacuum region of 20 Å. In calculations the bottom two layers for the Cu(111) slab and the bottom four layers for the Cu(110) slab were fixed, while all other atoms are fully relaxed. Only the Γ point was used for sampling the Brillouin zone of the slabs because of the large size of the supercell. An energy cutoff of 200 Ry was chosen to guarantee convergence of the total energies and forces. A common energy shift of 10 meV was applied. Self-consistency of the density matrix was achieved with a tolerance of 10^{-4}. For geometry optimization, the conjugate-gradient approach was used with a threshold of 0.02 eV Å^{-1}. The atoms in molecules (AIM) method of Bader was used for charge analysis.[57,58]

To obtain the most stable configurations of pristine, debrominated, and dehydrogenated DBBA on the Cu(111) and Cu(110) surfaces, a large number of the starting geometries (up to 30 for each molecule) in different nonequivalent positions and orientations were generated. The starting structures were optimized without any geometry constraints. A similar approach was successfully used in our previous works on adsorption, structure optimization, and catalytic reactions of various types of molecules and metal clusters on surfaces.[59−62]

Conflict of Interest: The authors declare no competing financial interest.

REFERENCES AND NOTES

1. Novoselov, K. S. A Roadmap for Graphene. *Nature* **2012**, *490*, 192−200.
2. Schwierz, F. Graphene Transistors. *Nat. Nanotechnol.* **2010**, *5*, 487−496.
3. Yang, L.; Park, C.-H.; Son, Y.-W.; Cohen, M. L.; Louie, S. G. Quasiparticle Energies and Band Gaps in Graphene Nanoribbons. *Phys. Rev. Lett.* **2007**, *99*, 186801.
4. Nguyen, L. T.; Pham, C. H.; Nguyen, V. L. Electronic Band Structures of Graphene Nanoribbons with Self-Passivating Edge Reconstructions. *J. Phys.: Condens. Matter* **2011**, *23*, 295503.
5. Bai, J.; Huang, Yu. Fabrication and Electrical Properties of Graphene Nanoribbons. *Mater. Sci. Eng., R* **2010**, *70*, 341−353.
6. Yazyev, O. V. A Guide to the Design of Electronic Properties of Graphene Nanoribbons. *Acc. Chem. Res.* **2013**, *46*, 2319−2328.
7. Son, Y.-W.; Cohen, M.; Louie, S. G. Half-Metallic Graphene Nanoribbons. *Nature* **2006**, *444*, 347−349.
8. Shemella, P.; Zhang, Y.; Mailman, M.; Ajayan, P. M.; Nayak, S. K. Energy Gaps in Zero-Dimensional Graphene Nanoribbons. *Appl. Phys. Lett.* **2007**, *91*, 042101.
9. Han, M. Y.; Özyilmaz, B.; Zhang, Y.; Kim, P. Energy Band-Gap Engineering of Graphene Nanoribbons. *Phys. Rev. Lett.* **2007**, *98*, 206805.
10. Cai, J.; Ruffieux, P.; Jaafar, R.; Bieri, M.; Braun, T.; Blankenburg, S.; Muoth, M.; Seitsonen, A. P.; Saleh, M.; Feng, X.; et al. Atomically Precise Bottom-Up Fabrication of Graphene Nanoribbons. *Nature* **2010**, *466*, 470−473.
11. Ruffieux, P.; Cai, J.; Plumb, N. C.; Patthey, L.; Prezzi, D.; Ferretti, A.; Molinari, E.; Feng, X.; Müllen, K.; Pignedoli, C. A.; et al. Electronic Structure of Atomically Precise Graphene Nanoribbons. *ACS Nano* **2012**, *6*, 6930−6935.
12. Linden, S.; Zhong, D.; Timmer, A.; Aghdassi, N.; Franke, J. H.; Zhang, H.; Feng, X.; Müllen, K.; Fuchs, H.; Chi, L.; et al. Electronic Structure of Spatially Aligned Graphene Nanoribbons on Au(788). *Phys. Rev. Lett.* **2012**, *108*, 216801.
13. Huang, H.; Wei, D.; Sun, J.; Wong, S. L.; Feng, Y. P.; Neto, A. H. C.; Wee, A. T. S. Spatially Resolved Electronic Structures of Atomically Precise Armchair Graphene Nanoribbons. *Sci. Rep.* **2012**, *2*, DOI: 10.1038/srep00983.
14. Talirz, L.; Söde, H.; Cai, J.; Ruffieux, P.; Blankenburg, S.; Jafaar, R.; Berger, R.; Feng, X.; Müllen, K.; Puasserone, D.; et al. Termini of Bottom-Up Fabricated Graphene Nanoribbons. *J. Am. Chem. Soc.* **2013**, *135*, 2060−2063.

15. Van der Lit, J.; Boneschanscher, M. P.; Vanmaekelbergh, D.; Ijäs, M.; Uppstu, A.; Ervasti, M.; Harju, A.; Liljeroth, P.; Swart, I. Suppression of Electron–Vibron Coupling in Graphene Nanoribbons Contacted *via* a Single Atom. *Nat. Commun.* **2013**, *4*, 2023.

16. Chen, Y.-C.; de Oteyza, D. G.; Pedramrazi, Z.; Chen, C.; Fischer, F. R.; Crommie, M. F. Tuning the Band Gap of Graphene Nanoribbons Synthesized from Molecular Precursors. *ACS Nano* **2013**, *7*, 6123–6128.

17. Cai, J.; Pignedoli, C. A.; Talirz, L.; Ruffieux, P.; Söde, H.; Liang, L.; Meunier, V.; Berger, R.; Li, R.; Feng, X.; et al. Graphene Nanoribbon Heterojunctions. *Nat. Nanotechnol.* **2014**, *9*, 896–900.

18. Simonov, K. A.; Vinogradov, N. A.; Vinogradov, A. S.; Generalov, A. V.; Zagrebina, E. M.; Mårtensson, N.; Cafolla, A. A.; Carpy, T.; Cunniffe, J. P.; Preobrajenski, A. B. Effect of Substrate Chemistry on the Bottom-Up Fabrication of Graphene Nanoribbons: Combined Core-Level Spectroscopy and STM Study. *J. Phys. Chem. C* **2014**, *118*, 12532–12540; *J. Phys. Chem. C* **2015**, *119*, 880–881(correction) .

19. Bronner, C.; Björk, J.; Tegeder, P. Tracking and Removing Br during the On-Surface Synthesis of a Graphene Nanoribbon. *J. Phys. Chem. C* **2015**, *119*, 486–493.

20. Chen, Y. C.; Cao, T.; Chen, C.; Pedramrazi, Z.; Haberer, D.; de Oteyza, D. G.; Fischer, F. R.; Louie, S. G.; Crommie, M. F. Molecular Bandgap Engineering of Bottom-Up Synthesized Graphene Nanoribbon Heterojunctions. *Nat. Nanotechnol.* **2015**, *10*, 156–160.

21. Massimi, L.; Ourdjini, O.; Lafferentz, L.; Koch, M.; Grill, L.; Cavaliere, E.; Gavioli, L.; Cardoso, C.; Prezzi, D.; Molinari, E.; et al. Surface-Assisted Reactions toward Formation of Graphene Nanoribbons on Au(110) Surface. *J. Phys. Chem. C* **2015**, *119*, 2427–2437.

22. Basagni, A.; Sedona, F.; Pignedoli, C. A.; Cattelan, M.; Nicolas, L.; Casarin, M.; Sambi, M. Molecules-Oligomers-Nanowires-Graphene Nanoribbons: a Bottom-Up Stepwise On-Surface Covalent Synthesis Preserving Long Range Order. *J. Am. Chem. Soc.* **2015**, *137*, 1802–1808.

23. Zhang, H.; Lin, H.; Sun, K.; Chen, L.; Zagranyarski, Y.; Aghdassi, N.; Duhm, S.; Li, Q.; Zhong, D.; Li, Y.; et al. On-Surface Synthesis of Rylene-Type Graphene Nanoribbons. *J. Am. Chem. Soc.* **2015**, *137*, 4022–4025.

24. Han, P.; Akagi, K.; Canova, F. F.; Mutoh, H.; Shiraki, S.; Iwaya, K.; Weiss, P. S.; Asao, N.; Hitosugi, T. Bottom-Up Graphene-Nanoribbon Fabrication Reveals Chiral Edges and Enantioselectivity. *ACS Nano* **2014**, *8*, 9181–9187.

25. Simonov, K. A.; Vinogradov, N. A.; Vinogradov, A. S.; Generalov, A. V.; Zagrebina, E. M.; Mårtensson, N.; Cafolla, A. A.; Carpy, T.; Cunniffe, J. P.; Preobrajenski, A. B. Comment on "Bottom-Up Graphene-Nanoribbon Fabrication Reveals Chiral Edges and Enantioselectivity. *ACS Nano* **2015**, *9*, 3399–3403.

26. Ullmann, F.; Bielecki, J. Ueber Synthesen in der Biphenylreihe. *Ber. Dtsch. Chem. Ges.* **1901**, *34*, 2174–2185.

27. Xi, M.; Bent, B. E. Mechanisms of the Ullmann Coupling Reaction in Adsorbed Monolayers. *J. Am. Chem. Soc.* **1993**, *115*, 7426–7433.

28. Grill, L.; Dyer, M.; Lafferentz, L.; Persson, M.; Peters, M. V.; Hecht, S. Nano-architectures by Covalent Assembly of Molecular Building Blocks. *Nat. Nanotechnol.* **2007**, *2*, 687–691.

29. Lipton-Duffin, J. A.; Ivasenko, O.; Perepichka, D. F.; Rosei, F. Synthesis of Polyphenylene Molecular Wires by Surface-Confined Polymerization. *Small* **2009**, *5*, 592–597.

30. Lafferentz, L.; Eberhardt, V.; Dri, C.; Africh, C.; Comelli, G.; Esch, F.; Hecht, S.; Grill, L. Controlling On-Surface Polymerization by Hierarchical and Substrate-Directed Growth. *Nat. Chem.* **2012**, *4*, 215–220.

31. Di Giovannantonio, M.; El Garah, M.; Lipton-Duffin, J.; Meunier, V.; Cardenas, L.; Fagot Revurat, Y.; Cossaro, A.; Verdini, A.; Perepichka, D. F.; Rosei, F.; et al. Insight into Organometallic Intermediate and its Evolution to Covalent Bonding in Surface-Confined Ullmann Polymerization. *ACS Nano* **2013**, *7*, 8190–8198.

32. Lewis, E. A.; Murphy, C. J.; Liriano, M. L.; Sykes, E. C. H. Atomic-Scale Insight into the Formation, Mobility and

33. Fan, Q.; Wang, C.; Liu, L.; Han, Y.; Zhao, J.; Zhu, J.; Kuttner, J.; Hilt, G.; Gottfried, J. M. Covalent, Organometallic, and Halogen-Bonded Nanomeshes from Tetrabromo-Terphenyl by Surface-Assisted Synthesis on Cu (111). *J. Phys. Chem. C* **2014**, *118*, 13018–13025.

34. Eichhorn, J.; Strunskus, T.; Rastgoo-Lahrood, A.; Samanta, D.; Schmittel, M.; Lackinger, M. On-Surface Ullmann Polymerization *via* Intermediate Organometallic Networks on Ag(111). *Chem. Commun.* **2014**, *50*, 7680–7682.

35. Bieri, M.; Nguyen, M. T.; Gröning, O.; Cai, J.; Treier, M.; Aït-Mansour, K.; Ruffieux, P.; Pignedoli, C. A.; Passerone, D.; Kastler, M.; et al. Two-Dimensional Polymer Formation on Surfaces: Insight Into the Roles of Precursor Mobility and Reactivity. *J. Am. Chem. Soc.* **2010**, *132*, 16669–16676.

36. Eichhorn, J.; Nieckarz, D.; Ochs, O.; Samanta, D.; Schmittel, M.; Szabelski, P. J.; Lackinger, M. On-Surface Ullmann Coupling: The Influence of Kinetic Reaction Parameters on the Morphology and Quality of Covalent Networks. *ACS Nano* **2014**, *8*, 7880–7889.

37. Gutzler, R.; Cardenas, L.; Lipton-Duffin, J.; El Garah, M.; Dinca, L. E.; Szakacs, C. E.; Fu, C.; Gallagher, M.; Vodráček, M.; Rybachuk; et al. Ullmann-Type Coupling of Brominated Tetrathienoanthracene on Copper and Silver. *Nanoscale* **2014**, *6*, 2660–2668.

38. Koch, M.; Gille, M.; Viertel, A.; Hecht, S.; Grill, L. Substrate-controlled linking of molecular building blocks: Au (111) *vs.* Cu (111). *Surf. Sci.* **2014**, *627*, 70–74.

39. Pinardi, A. L.; Otero-Irurueta, G.; Palacio, I.; Martinez, J. I.; Sanchez-Sanchez, C.; Tello, M.; Rogero, C.; Cossaro, A.; Preobrajenski, A.; Gómez-Lor, B.; et al. Tailored Formation of N-Doped Nanoarchitectures by Diffusion-Controlled on-Surface (Cyclo) Dehydrogenation of Heteroaromatics. *ACS Nano* **2013**, *7*, 3676–3684.

40. Peljhan, S.; Kokalj, A. DFT Study of Gas-Phase Adsorption of Benzotriazole on Cu(111), Cu(100), Cu(110), and Low Coordinated Defects Thereon. *Phys. Chem. Chem. Phys.* **2011**, *13*, 20408–20417.

41. Hu, Z. X.; Lan, H.; Ji, W. Dissociative Adsorption of CH_3X (X= Br and Cl) on a Silicon (100) Surface Revisited by Density Functional Theory. *Sci. Rep.* **2014**, *4*, 5036.

42. Haq, S.; Hanke, F.; Sharp, J.; Persson, M.; Amabilino, D. B.; Raval, R. Versatile Bottom-Up Construction of Diverse Macromolecules on a Surface Observed by Scanning Tunneling Microscopy. *ACS Nano* **2014**, *8*, 8856–8870.

43. Kuck, S.; Prostak, M.; Funk, M.; Bröring, M.; Hoffmann, G.; Wiesendanger, R. Disposition of the Axial Ligand in the Physical Vapor Deposition of Organometallic Complexes. *J. Vac. Sci. Technol., A* **2010**, *28*, 795–798.

44. Klues, M.; Hermann, K.; Witte, G. Analysis of the Near-Edge X-ray-Absorption Fine-Structure of Anthracene: A Combined Theoretical and Experimental Study. *J. Chem. Phys.* **2014**, *140*, 014302.

45. Dyer, M. S.; Robin, A.; Haq, S.; Raval, R.; Persson, M.; Klimeš, J. Understanding the Interaction of the Porphyrin Macrocycle to Reactive Metal Substrates: Structure, Bonding, and Adatom Capture. *ACS Nano* **2011**, *5*, 1831–1838.

46. Jones, R. G.; Kadodwala, M. Bromine Adsorption on Cu(111). *Surf. Sci.* **1997**, *370*, 219–225.

47. Lacovig, P.; Pozzo, M.; Alfe, D.; Vilmercati, P.; Baraldi, A.; Lizzit, S. Growth of Dome-Shaped Carbon Nanoislands on Ir(111): the Intermediate Between Carbidic Clusters and Quasi-Free-Standing Graphene. *Phys. Rev. Lett.* **2009**, *103*, 166101.

48. Adams, D. L. *FitXPS*, v 2.12; available from www.sljus.lu.se/download.html.

49. Horcas, I.; Fernández, R.; Gómez-Rodriguez, J. M.; Colchero, J.; Gómez-Herrero, J.; Baro, A. M. WSXM: a Software for Scanning Probe Microscopy and a Tool for Nanotechnology. *Rev. Sci. Instrum.* **2007**, *78*, 013705.

50. Wu, Z.; Cohen, R. E. More Accurate Generalized Gradient Approximation for Solids. *Phys. Rev. B: Condens. Matter Mater. Phys.* **2006**, *73*, 235116.

51. Soler, J. M.; Artacho, E.; Gale, J. D.; García, A.; Junquera, J.; Ordejón, P.; Sánchez-Portal, D. The SIESTA Method for *ab initio* Order-N Materials Simulation. *J. Phys.: Condens. Matter* **2002**, *14*, 2745–2779.
52. Tran, F.; Laskowski, R.; Blaha, P.; Schwarz, K. Performance on Molecules, Surfaces, and Solids of the Wu-Cohen GGA Exchange-Correlation Energy Functional. *Phys. Rev. B: Condens. Matter Mater. Phys.* **2007**, *75*, 115131.
53. Laskowski, R.; Blaha, P.; Schwarz, K. Bonding of Hexagonal BN to Transition Metal Surfaces: An *ab Initio* Density-Functional Theory Study. *Phys. Rev. B: Condens. Matter Mater. Phys.* **2008**, *78*, 045409.
54. Troullier, N.; Martins, J. L. Efficient Pseudopotentials for Plane-Wave Calculations. *Phys. Rev. B: Condens. Matter Mater. Phys.* **1991**, *43*, 1993–2006.
55. Monkhorst, H. J.; Pack, J. D. Special Points for Brillouin-Zone Integrations. *Phys. Rev. B* **1976**, *13*, 5188.
56. Wyckoff, R. W. G. *Crystal Structures*; John Wiley & Sons: New York, 1963; Vol. 1.
57. Bader, R. *Atoms in Molecules: A Quantum Theory*; Oxford University Press: New York, 1990.
58. Henkelman, G.; Arnaldsson, A.; Jónsson, H. A Fast and Robust Algorithm for Bader Decomposition of Charge Density. *Comput. Mater. Sci.* **2006**, *36*, 354–360.
59. Lyalin, A.; Nakayama, A.; Uosaki, K.; Taketsugu, T. Functionalization of Monolayer h-BN by a Metal Support for the Oxygen Reduction Reaction. *J. Phys. Chem. C* **2013**, *117*, 21359–21370.
60. Uosaki, K.; Elumalai, G.; Noguchi, H.; Masuda, T.; Lyalin, A.; Nakayama, A.; Taketsugu, T. Boron Nitride Nanosheet on Gold as an Electrocatalyst for Oxygen Reduction Reaction: Theoretical Suggestion and Experimental Proof. *J. Am. Chem. Soc.* **2014**, *136*, 6542–6545.
61. Lyalin, A.; Nakayama, A.; Uosaki, K.; Taketsugu, T. Adsorption and Catalytic Activation of the Molecular Oxygen on the Metal Supported h-BN. *Top. Catal.* **2014**, *57*, 1032–1041.
62. Gao, M.; Lyalin, A.; Taketsugu, T. CO Oxidation on h-BN Supported Au Atom. *J. Chem. Phys.* **2013**, *138*, 034701.